Magnetic Flux Cancellation in Ellerman Bombs

The Astrophysical Journal, 823:110 (10pp), 2016 June 1 doi:10.3847/0004-637X/823/2/110

MAGNETIC FLUX CANCELLATION IN ELLERMAN BOMBS

A. Reid[1,2], M. Mathioudakis[1], J. G. Doyle[2], E. Scullion[3], C. J. Nelson[1,4], V. Henriques[1], and T. Ray[5]
[1] Astrophysics Research Centre, School of Mathematics and Physics, Queen's University Belfast, BT7 1NN, Northern Ireland, UK; areid29@qub.ac.uk
[2] Armagh Observatory, College Hill, Armagh, BT61 9DG, UK
[3] Trinity College Dublin, College Green, Dublin 2, Ireland
[4] Solar Physics and Space Plasma Research Centre, University of Sheffield, Hicks Building, Hounsfield Road, Sheffield, S3 7RH, UK
[5] Dublin Institute for Advanced Studies, 31 Fitzwilliam Place, Dublin 2, Ireland
Received 2015 November 17; accepted 2016 March 22; published 2016 May 27

ABSTRACT

Ellerman Bombs (EBs) are often found to be co-spatial with bipolar photospheric magnetic fields. We use Hα imaging spectroscopy along with Fe I 6302.5 Å spectropolarimetry from the Swedish 1 m Solar Telescope (SST), combined with data from the *Solar Dynamic Observatory*, to study EBs and the evolution of the local magnetic fields at EB locations. EBs are found via an EB detection and tracking algorithm. Using NICOLE inversions of the spectropolarimetric data, we find that, on average, $(3.43 \pm 0.49) \times 10^{24}$ erg of stored magnetic energy disappears from the bipolar region during EB burning. The inversions also show flux cancellation rates of 10^{14}–10^{15} Mx s^{-1} and temperature enhancements of 200 K at the detection footpoints. We investigate the near-simultaneous flaring of EBs due to co-temporal flux emergence from a sunspot, which shows a decrease in transverse velocity when interacting with an existing, stationary area of opposite polarity magnetic flux, resulting in the formation of the EBs. We also show that these EBs can be fueled further by additional, faster moving, negative magnetic flux regions.

Key words: magnetic reconnection – Sun: atmosphere – Sun: magnetic fields – Sun: photosphere

Supporting material: animation

1. INTRODUCTION

Ellerman Bombs (EBs) are small-scale, short-lived, impulsive brightenings that were originally detected in the outer wings of the Hα line (Ellerman 1917). They occur exclusively near solar active regions (Zachariadis et al. 1987; Georgoulis et al. 2002) or areas of enhanced photospheric magnetic activity (e.g., Pariat et al. 2004; Watanabe et al. 2008). The Hα line profile of an EB has an absorption core, which remains unchanged relative to the local background, and emission in the line wings during the lifetime of the EB. The emission wings may be asymmetric, which could be due to overlying chromospheric flows (Bruzek 1972; Kitai 1983; Dara et al. 1997; Watanabe et al. 2011; Vissers et al. 2013). EBs also appear in Ca II 8542 Å with line profile characteristics similar to those in Hα (Fang et al. 2006; Socas-Navarro et al. 2006; Pariat et al. 2007; Vissers et al. 2013; Li et al. 2015). EBs are thought to produce no observable effects in the upper atmosphere (Vissers et al. 2013), although there may be some tentative indications of heated areas of the transition region above the location of EB activity (Schmieder et al. 2004). Brightenings from EBs have also been observable in the *Solar Dynamic Observatory* (*SDO*) 1700 and 1600 Å channels, though to a lesser degree than the Hα line wings due to the broad passbands of these filters encompassing a wide range of atmospheric heights (Vissers et al. 2013). While the 1600 Å channel offers a better contrast as opposed to the 1700 Å channel (Rutten et al. 2013; Vissers et al. 2013), the EB signatures are more difficult to observe in the 1600 Å channel due to contamination effects from C IV emission with transition region temperatures.

More recent studies involving the Interface Region Imaging Spectrograph explorer find "bombs" in atmospheric lines such as Si IV, C II, and Mg II, indicating that these regions are host to pockets of hot plasma with possible temperatures ranging from 6000 to 80,000 K and bi-directional flows of up to 80 km s^{-1} (Peter et al. 2014). These "bombs" have been observed co-spatially with EBs found in Hα by Vissers et al. (2015), and now hint that the tops of EBs may be heated to transition region temperatures at physical heights below the chromospheric canopy, bringing into question the previous temperature estimates from modeling EBs. However, Judge (2015) debated the origins of these "bombs," speculating that their formation is due to Alfvénic turbulence in the low-mid chromosphere.

Several studies of EBs connect their detection in Hα with regions of opposite polarity photospheric magnetic fields (Georgoulis et al. 2002; Matsumoto et al. 2008b; Watanabe et al. 2008; Hashimoto et al. 2010; Nelson et al. 2013b; Vissers et al. 2013). More recent studies also hint at the possible flux cancellation of the bipoles at EB sites (Matsumoto et al. 2008b; Nelson et al. 2013b; C. J. Nelson et al. 2016, in preparation) with values for flux cancellation in the region of $(3–8.5) \times 10^{14}$ Mx s^{-1}. It is thought that this flux cancellation in the form of photospheric magnetic reconnection is the driver behind the appearance of EBs (Georgoulis et al. 2002; Isobe et al. 2007; Matsumoto et al. 2008a, 2008b; Watanabe et al. 2008; Hashimoto et al. 2010). It has been shown numerically that photospheric magnetic reconnection would be most efficient at the temperature minimum at a height of 600 km above the lower photospheric boundary (Litvinenko 1999). EBs have been estimated to form at this height (Nelson et al. 2015), with footpoints reported to form as low as the intergranular lanes near the photospheric floor (Watanabe et al. 2011).

There are three main mechanisms related to EB events and their associated magnetic topologies. Two of these mechanisms involve reconnection between areas of opposite polarity magnetic flux. The first of these is triggered by the emergence of new flux interacting with an existing area of opposite

polarity (Watanabe et al. 2008; Hashimoto et al. 2010). The second mechanism involves reconnection along a resistive, undulatory "sea serpent" flux emergence (Georgoulis et al. 2002; Pariat et al. 2004). The final mechanism does not involve opposite polarity reconnection, and instead the EB is caused by shearing reconnection in a unipolar region of magnetic flux (Georgoulis et al. 2002; Watanabe et al. 2008).

Three-dimensional numerical modeling of the "sea serpent" reconnection case has been studied, showing a local temperature increase ratio in the photosphere of 1.1–1.5 relative to the quiet Sun, along with a density increase by a factor of 4 at the reconnection site (Archontis & Hood 2009). The Archontis & Hood (2009) model has also shown bi-directional flows in the region with values of 2–4 km s^{-1}. Semi-empirical models for EBs show localized temperature enhancements of 600–3000 K around the temperature minimum region (Fang et al. 2006; Berlicki & Heinzel 2014). These temperature enhancements lead to intensity enhancements in the wings of the Hα and Ca II 8542 Å lines, while the line cores are formed higher in the chromosphere. Other studies of EBs also find similar temperature enhancements ranging from 200 to 3000 K in the photosphere/temperature minimum region (Georgoulis et al. 2002; Isobe et al. 2007; Yang et al. 2013; Hong et al. 2014; Li et al. 2015).

The radiative energies of EBs have also been considered by estimating the radiative loss rate from Hα. Assuming an EB lifetime of 600 s, with a depth of 100 km, and measuring the apparent area of the brightenings, Georgoulis et al. (2002) found that EBs have a total radiative energy of 10^{27}–10^{28} erg with peak energy rates of 10^{25} erg s^{-1}. The statistical study of Nelson et al. (2013a) applied a similar method to the results of an automated detection algorithm for EBs and found a lower total radiative energy of 10^{22}–10^{25} erg, with peak radiative loss rates of 10^{21}–10^{23} erg s^{-1}.

In this paper, we use high spatial and temporal resolution Hα imaging spectroscopy along with Fe I 6302.5 Å imaging spectropolarimetry from the Swedish 1 m Solar Telescope (SST) to study EBs and their associated flux cancellation rates. The EBs are detected and tracked using an automated algorithm. The identified features are then inverted using NICOLE to produce estimated flux cancellation rates and temperature information.

2. OBSERVATIONS AND DATA REDUCTION

The observations were carried out with the CRisp Imaging SpectroPolarimeter (CRISP) at the SST (Scharmer et al. 2003, 2008) on La Palma. The target was active region NOAA 12077, near the disk center (coordinates: $X = 180''$, $Y = -81''$, $\mu = 0.97$). The observations took place on 2014 June 5 between 08:27 and 09:58 UT. The observational setup was comprised of Hα line scans using 5 points of ±1.032 Å, ±0.774 Å, and the line core, imaging spectropolarimetry in Fe I 6302 Å, sampled across 11 points ranging from ±0.15 Å from the line center, in steps of 30 mÅ. An Fe I scan was taken after every 9 Hα scans. The spectropolarimetric data had a post-reduction mean cadence of 45 s, while the Hα spectral imaging had a mean cadence of 3.2 s, with 17 s cadence when the Fe I data was being acquired. The image scale of the observations was $0''.059$ $pixel^{-1}$, with a total field of view (FOV) of $59'' \times 58''$. A snapshot of the FOV is shown in Figure 1.

The data were processed with the Multi-object Multi-frame Blind Deconvolution (MOMFBD) algorithm (van Noort et al. 2005). This includes tessellation of the images into 64 × 64 $pixels^2$ sub-images for individual restoration, performed over each temporal frame and line position within the scans. Wide-band images act as a stabilizer for the narrow-band alignment causing the different polarimetric states to be consistent, seeing and reconstruction-wise, and thus preventing seeing-induced cross-talk during demodulation (Henriques 2012). Prefilter FOV and wavelength-dependent corrections were applied to the restored images. The spectropolarimetric data were also demodulated to remove the cross-talk between the Stokes parameters (Schnerr et al. 2011). The final correction involved the long-scale cavity error of the instrument. Further information on the MOMFBD image restoration techniques is available in van Noort & Rouppe van der Voort (2008) and de la Cruz Rodríguez et al. (2015).

The SST observations were combined with data from the 1700 Å passband of the Atmospheric Imaging Assembly (AIA; Lemen et al. 2012) and Helioseismic Magnetic Imager (HMI; Scherrer et al. 2012) on the *SDO*. These were reduced and cropped temporally to match the timestamps of the Hα SST data cube as closely as possible for AIA. The HMI magnetograms were temporally aligned to the timestamps of the spectropolarimetric data. The *SDO* data were then spatially aligned to the SST data. This was done by centering the *SDO* data cubes on the center pointing value from the SST. The *SDO* data were scaled to match the pixel resolution of SST and, finally, rotated with respect to the observation angle of the SST data. The accuracy of the alignment for the data was checked by comparing the central positions of the dark sunspot regions with the Hα −1.032 Å images. After this, a co-aligned datacube was made for the 1700 Å AIA data and magnetograms, with finer calibrations to the alignment made manually for each channel, for the whole timeseries. Aligned frames of the full FOV are shown in Figure 1.

3. EB DETECTION AND TRACKING

The detection of EBs was carried out with an EB Detection Automation and Tracking Algorithm (EBDATA). For a feature to be classified as an EB, it has to fulfill the following criteria.

1. The feature must have at least one pixel with intensity >145% that of the local quiet Sun in both wings of Hα at ±1.032 Å.
2. The surrounding area is grown to an intensity threshold of >130% using the same quiet-Sun profile above at the same wavelength positions. The grown area has to be greater than 15 pixels.
3. The line core in Hα must remain unchanged (no more than 10% increase to account for variability) relative to the average line core intensity at the EB location over the previous 60 s.
4. The temporal variation of the intensity must show evidence of impulsivity (10% increase in the intensity in the grown EB area over the previous 60 s).
5. The lifetime of the event needs to be >45 s.

The first two criteria use intensity thresholding to identify possible candidates, similar to Vissers et al. (2013), though with lower intensities. The lower intensities were chosen because the average value is taken over an area of quiet Sun, not the full FOV, and so in discounting the sunspot, the relative average increases. The quiet-Sun profile was taken over an area of 200 $pixels^2$ ($11.84''^2$), centered about the position $X =$

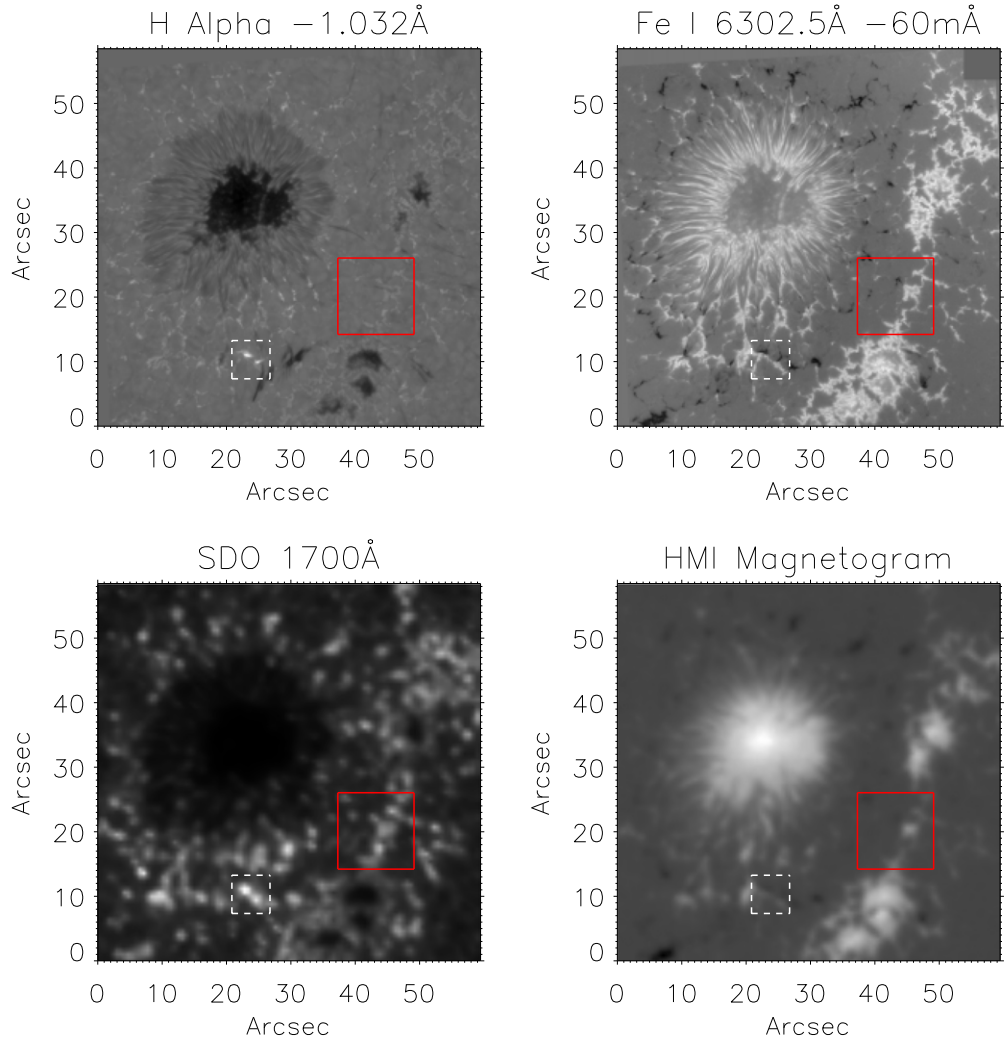

Figure 1. Top left: Hα image −1.032 Å from line center showing the FOV of the SST. Two flaring EBs can be seen (highlighted white dashed box). The red solid box shows the area of quiet Sun used for reference. Top right: co-spatial and co-temporal Stokes-*V* image. Bottom left: co-spatial *SDO* 1700 Å snapshot. Bottom right: co-spatial HMI line-of-sight magnetogram.

43.″216, $Y = 20.''128$, seen in the red box of Figure 1. The intensity threshold for the grown area is the same as that of Nelson et al. (2013a). The size criterion was added to ensure that no small-scale anomalies were picked up as detections. Detection criterion 4 calls for the potential EB to show impulsivity to ensure that no moving magnetic features were falsely identified (pseudo-EBs; Rutten et al. 2013). EBs are impulsive reconnection events and should exhibit some form of flaring as one of their main signatures (Watanabe et al. 2011; Rutten et al. 2013; Vissers et al. 2013; Reid et al. 2015). This intensity change was to be only in the wings and not in the core of Hα. The intensity change is averaged over the whole grown area and is a running average.

If detection criteria 1–3 are met, then the detected area is placed into a detection binary cube. This datacube then runs through the tracking algorithm. The algorithm looks at the detections in each timeframe. The first frame containing detections will label each detection area in the binary map with a tracking number. Tracking numbers are only assigned if the impulsivity criterion is fulfilled. Subsequent frames are then scanned for individual detections and the pixels within each detection are checked for any overlap with labeled EBs within the previous 60 s to allow for lapses in seeing. If a detection shows any overlap with a previously labeled EB, then the detection is labeled with the overlapping tracking number (if there are multiple overlapped numbers, then it takes the tracking number of the one with the highest correlation). After this, a clean up routine is performed which removes any detection with a lifetime less than 45 s (criterion 5).

The output of EBDATA provides the user with the sizes, positions, and mean intensity values relative to the averaged background for each detection, along with an EB detection cube showing where each detection is and its tracking number on the data set. The outputs can be used to determine lifetimes, apparent transverse velocities, maximum detected intensities (averaged peak intensity over all detected pixels), and sizes (see Figure 2).

Running this detection and tracking algorithm, we find 116 EBs in the entire Hα data set. For comparison, the algorithm was also run with the impulsivity criteria switched off. This resulted in 151 EB detections, though when comparing the statistical characteristics of the two sets of results, they were very similar. The additional detections appeared to be short lived, small scale, and with lower average intensity (see panels

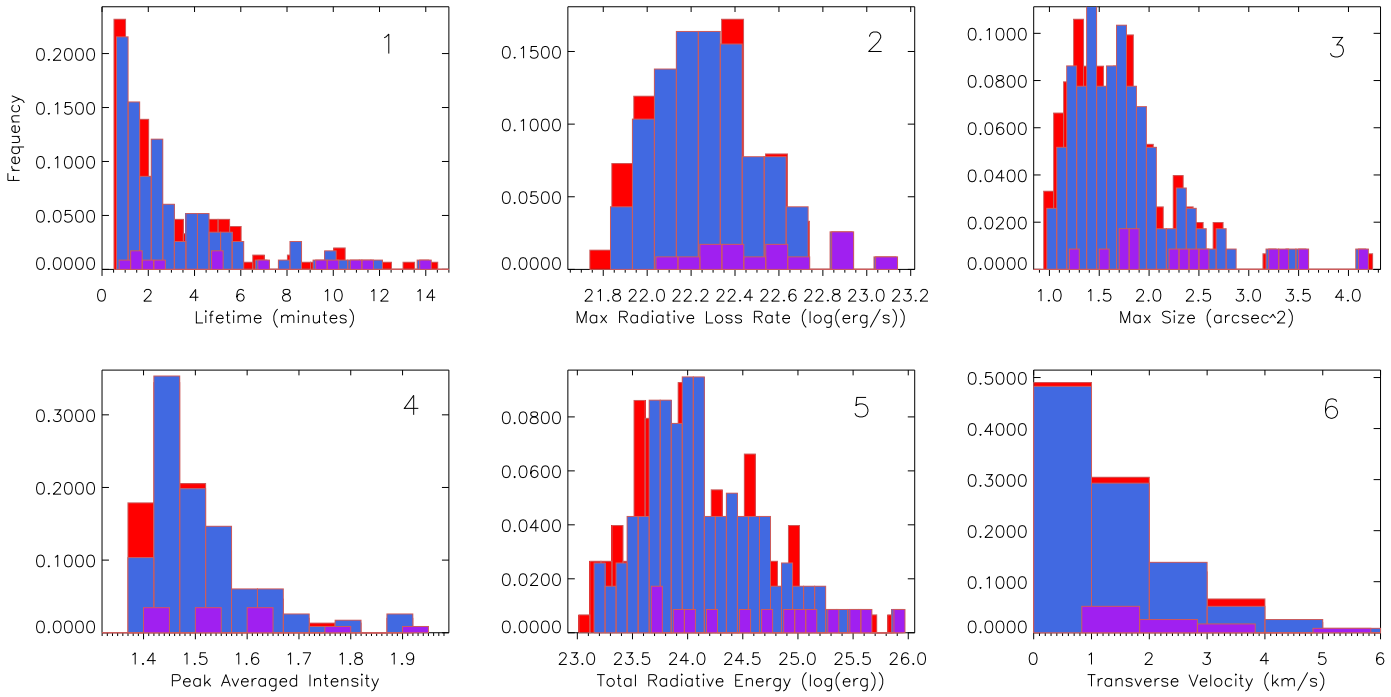

Figure 2. Histograms of the EBDATA output with the impulsiveness criterion activated (blue) and deactivated (red) for comparison. The purple bins correspond to the 14 detections from the blue bins which were chosen for inversions (see Section 4).

(1), (3), and (4) of Figure 2). This provides some reassurance that the impulsivity criterion removes pseudo-EBs.

The energy of each detection was also estimated. This was done by adopting the method of Georgoulis et al. (2002), who adopt the expression for radiative loss rate per unit volume from Nagai et al. (1980) as

$$\varepsilon_{\rm rad} \simeq a(T) n^2 \chi g(T), \quad (1)$$

where χ is the ionization degree, from Brown (1973), which requires estimates of the local density and temperature. Assuming $n \simeq 10^{12}\,{\rm cm}^{-3}$ and $T \simeq 10^4\,{\rm K}$, the ionization degree for the EB was estimated to be $\chi \simeq 0.89$. Using Nagai et al. (1980) to obtain the value of $a(T) \simeq 0.1$ for $T \simeq 10^4\,{\rm K}$, they find that the radiative loss rate per unit volume is $\varepsilon_{\rm rad} \simeq 0.89\,{\rm erg\,cm^{-3}\,s^{-1}}$. Using this, a peak radiative energy rate could be calculated via

$$P_{\rm rad} = \varepsilon_{\rm rad} f V_{\rm EB}, \quad (2)$$

where f is the filling factor (assumed to be unity) and $V_{\rm EB}$ is the maximum volume of the EB. The volume of the EB was gathered by taking the apparent area encasing the brightening of the EB, and assuming a constant depth of 100 km. Under the assumption that the EB has an equal rising and decaying phase, with a total EB lifetime of D, the total energy could be calculated as

$$E_{\rm rad} \sim \frac{P_{\rm rad} D}{2}. \quad (3)$$

The method above is used with the output of EBDATA using an estimated vertical extent for the EB of ≈400 km for Equation (2). This is a rough average of the temperature bump widths from semi-empirical modeling (Fang et al. 2006; Berlicki & Heinzel 2014; Li et al. 2015) and observed peak extents of EBs (Watanabe et al. 2011; Nelson et al. 2015). Temperature and density estimates are taken from Georgoulis et al. (2002), which are needed to estimate the net radiative loss rate. The total energy (panel (5) of Figure 2) is then estimated by integrating all of the calculated energies from the beginning to the end of the detection. The peak energy rates (panel (2) of Figure 2) are 10^{22}–$10^{23}\,{\rm erg\,s^{-1}}$ with total radiative energies ranging between 10^{23} and $10^{26}\,{\rm erg}$.

Our algorithm was adapted to allow for comparison with previous detection algorithms. Nelson et al. (2013a) found 3570 EBs in a $58'' \times 58''$, 90 minute long data set of a sunspot. The majority of these detections have since been classified as pseudo-EBs (Rutten et al. 2013). Adapting our algorithm to match their criteria yields 3294 detections, most of which are extremely short-lived, small-scale, low-intensity brightenings. Nelson et al. (2013a) found 0.684 detections arcsec^{-2} s^{-1}, while our adaptation yielded 0.618 detections arcsec^{-2} s^{-1}. Vissers et al. (2013) also created a detection algorithm, identifying 139 potential EBs in two data sets of $54'' \times 53''$ lasting a total of 106 minutes (0.245 detections arcsec^{-2} s^{-1}). For the data set presented in this paper, the Vissers et al. (2013) criteria yielded 130 potential EBs, corresponding to 0.244 detections arcsec^{-2} s^{-1}. The 130 detections is fairly similar to the 116 detected using the criteria adopted in this work. When comparing the statistical characteristics of the detections between the 130 and the 116 potential EBs presented for this paper, they were extremely similar, with the extra detections appearing to be small in size (thin long brightenings), with a short lifetime, and velocity.

As mentioned earlier, our observations included the Fe I 6302.5 Å line in spectropolarimetry mode. We checked how many detections overlapped areas of strong photospheric line-of-sight magnetic field, and how many overlapped with areas of opposite polarity magnetic flux. This was carried out with a 20 pixel^2 (roughly $1\farcs2 \times 1\farcs2$) area around the center of each detection in the Stokes-V signal where we checked for strong

Table 1
The Results of Our Detection and Tracking Algorithm (EBDATA), using Various Detection Criteria, with Relative Magnetic Field Information

Algorithm	Detections	Bipoles (%)	Strong B Fields (%)
Reid	116	68 (58.6)	102 (87.9)
Vissers	130	75 (57.7)	114 (87.6)
Nelson	3294	874 (26.5)	2492 (75.6)
Reid (NI)	151	77 (50.1)	131 (86.7)

Note. NI stands for Non-impulsive where the impulsivity criterion was disabled.

signal in both polarities. A threshold was set to help define what is a strong field, and was considered to be anything with an absolute value greater than the standard deviation of the whole FOV at −60 mÅ from the line center. This wavelength was chosen to correspond best to the peak of the Stokes-V signal, showing the best contrast for line-of-sight magnetic fields (similar to Vissers et al. 2013, but note the difference in spectral resolution). If a sufficient number of pixels (>25%) was found in the box that met this threshold, then a strong field was assumed to exist. If strong fields were present in both polarities, then bipoles were considered to be present. The results in Table 1 show that including the impulsivity criterion reduces the number of detections, while strengthening the proportion of detections with associated bipoles.

4. PHOTOSPHERIC INVERSIONS AND MAGNETIC FLUX CANCELLATION

The NICOLE inversion code (Socas-Navarro et al. 2015) was used to determine the evolution of the magnetic flux at the EB locations. NICOLE is a parallelized code which solves multi-level, non-LTE problems following the preconditioning approach described in Socas-Navarro & Trujillo Bueno (1997), and which allows for inversions of Stokes profiles which may contain Zeeman-induced polarization by using response functions combined with standard fitting techniques (Socas-Navarro et al. 1998). The inversions require an initial model to be perturbed, which contains parameters such as a temperature profile, line-of-sight velocity, magnetic field vector, density, and microturbulence. Our initial guess model is taken to be the FAL-C atmosphere (Fontenla et al. 1993). The inversion code attempts to minimize the difference between the observations and the synthetic profiles, which leads to an inverted model of the observed atmosphere.

The electron and gas pressures are attained from inserting the temperature stratification into an equation of state with hydrostatic equilibrium imposed and an upper boundary for the electron pressure. As a result, it may not be possible to obtain flows in the inversion outputs of EBs, as would be expected in the real case (Berlicki & Heinzel 2014). NICOLE currently has no alternatives other than hydrostatic equilibrium to obtain pressures in inversion mode, and while EBs are impulsive dynamical brightenings, the local magnetic flux output should not be affected.

Isotropic scattering and complete frequency redistribution are also assumed by NICOLE. While NICOLE uses a plane parallel atmosphere, radiation comes from and scatters in all directions ($I-$ and $I+$) with each direction seeing a different effective atmosphere. The correct radiation field is important when computing the NLTE populations of the different levels. NICOLE supports up to five angles along a Gaussian quadrature (see, e.g., Section 5.1.2 of Rutten 2003 for further details of such numerical approximation in this context). We selected three angles, which is a common compromise between accuracy and speed.

This atmosphere is perturbed in a depth-dependent fashion by the use of response functions to converge to a point where the synthetic Stokes output is most similar to the observed profiles for that pixel.

Due to NICOLE inversions being computationally intensive, and the possibility that some of the weaker, shorter-lived EBDATA detections could be pseudo-EBs, not all 116 detections were inverted. This number was reduced by looking into EB appearances in *SDO*/AIA channels.

Vissers et al. (2013) tested their algorithm on the *SDO* 1700 Å AIA channel by using an intensity threshold of 5σ above average instead of the 155%/140% thresholding for Hα. They found a much lower number of EBs than in the Hα observations, noting that only the more pronounced EBs were detected in 1700 Å. Here, we have adopted a similar approach. Using co-aligned *SDO* 1700 Å data, a binary map was created for pixels that were 5σ above the average intensity in each frame. In addition, EBs which are only detected near the end of the observations are also discounted, as the purpose of this study is to investigate the change in photospheric magnetic fields over time at EB locations. This narrowed down the 116 detections to just 14, of which 13 contained overlapping opposite polarity photospheric magnetic flux, checked via 6302.5 Å Stokes-V, with one detection containing an apparent unipolar region. These were then split into two subsets, with the primary subset containing all of the detections which show up with the 1700 Å intensity threshold above 6σ, and a secondary set of detections which pass the 5σ thresholding, but not above 6σ.

We inverted 100×100 pixel^2 around each detection. Inversions were done for the EBs relative to their detected start times. Six frames were inverted for each EB, beginning six scans prior to the detection, in steps of six scans, up to 18 frames after the initial detection. The sixth inverted frame was the final detected frame. Only six frames were chosen to show the flux changing over time while not being extremely intensive. The observations were prepared for NICOLE by normalizing the observed profiles to the ±150 mÅ averaged values and interpolating the data points of the spectra to a finer grid. The latter allows enough points for NICOLE to fit the synthetic spectra and it allows the use of the cubic DELO-Bezier formal solver as described in de la Cruz Rodrguez & Piskunov (2013). To maximize the sensitivity to the data, the weights for the interpolated spectral-points not corresponding to an observed wavelength were assigned a negligible, non-zero weight.

The NICOLE inversions used three nodes in temperature, one in line-of-sight velocity, and one in vertical line-of-sight magnetic flux density (one node implies that there will be no fitting of these parameters with height). These numbers were chosen to give simple, effective values of magnetic field and temperature without introducing increased inversion noise, which would then result in fewer successfully inverted pixels in the EB locations. For the final inversions, no nodes were added for transverse magnetic fields to reduce inversion noise. One test inversion was performed with transverse magnetic field components, which resulted in little transverse fields at the

magnetic inversion line, and so we assume here that the majority of the magnetic flux is vertical. This also allows for a direct comparison with the HMI line-of-sight magnetograms. Stray light was not added, as this produced incorrect fits and dramatically increased the inversion noise. This is probably due to the high correlation of the stray-light profile with the data itself, allowing for very good but incorrect fits by perturbing the stray-light component alone. Stray light is a major component of all observations, having a similar impact on the contrast of both ground-based (Scharmer et al. 2011) and space-based observations (Danilovic et al. 2008). The observed noise, when fitting stray-light in this work, strongly suggests that spatially coupled inversions (similar to van Noort 2012, but with an unknown PSF) would greatly constrain the stray-light fitting, and thus lead to greatly improved results. NICOLE currently does not have the ability to perform spatially coupled inversions.

We also attempted to add a microturbulence parameter to the fitting. This showed results very similar to the inversions without microturbulence, but with better fitting of the Stokes profiles. EBs are impulsive events that are dominated by large heating and increased magnetic flux in the upper photosphere. While successfully inverted pixels produced better fits, the microturbulence results do not seem to capture such variability, and instead lead to less successfully inverted pixels.

Figure 3 shows example output model data from the inversions with the original SST observations for EBDATA detection 091. At the location of the brightening in Hα, a temperature rise is visible in the models of roughly 1800 K above the FAL-C temperature at the detection footpoint (log (τ) = -1; a 490 K increase locally compared to 265 s before the detection occurred). The output model also shows a clear bipolar region, shown in the line-of-sight magnetic field map, with absolute flux densities of around 1 kG. There is a second bipolar region in the bottom right corner of the observations and output model, which forms detection 092, roughly 13 s after this snapshot, and is discussed in the next section. With only one node in the line-of-sight velocity, we have no information on the velocity gradient as a function of height. There is no evidence for strong velocity fields in the output model.

All 14 detections were inverted using the procedure described above. The results show flux cancellation at the primary EB locations with an average rate of $(1.01 \pm 0.14) \times 10^{15}$ Mx s^{-1}. One of the primary detections shows an increase in magnetic flux. All of the flux cancelation measurements were made with a $1\farcs8 \times 1\farcs8$ box created around the detection location, measured from the initial frame to the final frame of the associated detection. The uncertainties are calculated from the noise of the FOV. The secondary detections show an average flux cancellation rate of $(7.73 \pm 1.13) \times 10^{14}$ Mx s^{-1}, with two of the secondary detections showing a small increase in the local magnetic flux. The increase comes from the negative polarity, while the positive polarity areas experience flux cancellation with every EB detection. The negative polarity magnetic flux increases occur in many of the 14 detections and is due to areas of negative polarity magnetic flux moving into the area of the EB, continuously feeding the flux into the magnetic inversion line (see attached Movie for example). The positive flux areas are mostly stationary over time. The positive flux cancellation over all 14 detections occured at a rate of $(1.12 \pm 0.16) \times 10^{15}$ Mx s^{-1}, which can be compared to the average total flux cancellation rate of $(9.17 \pm 1.26) \times 10^{14}$ Mx s^{-1}.

The flux cancellation rate was also measured using co-aligned HMI line-of-sight magnetograms. In HMI, the primary detections had an average flux cancellation rate of $(1.25 \pm 0.25) \times 10^{15}$ Mx s^{-1}, while the weaker, secondary detections had a lower rate of $(6.73 \pm 1.41) \times 10^{14}$ Mx s^{-1}. Both HMI measurements and the inversion measurements show similar results, with an average increase in negative polarity flux and an overall average decrease in positive polarity flux.

Magnetic energies were also estimated, from the same area as the flux cancellation measurements, using the following equation:

$$E_B = (S\, dlB^2/2\mu), \tag{4}$$

where S is the apparent area of the magnetic flux around the detection, and dl is the estimated vertical extent of the EB, assumed to be 400 km (the same as the depth for the radiative energy calculations in Section 3). The magnetic permeability was assumed to be $4\pi \times 10^{-7}$ N A^{-2}.

The magnetic energies estimated for the detections were in the region 10^{24}–10^{25} erg. The difference in magnetic energies over time was also calculated by measuring the magnetic energy difference in the box from the initial detection time to the last inverted frame of the detection. For the primary detections, the magnetic energy difference averaged $(3.91 \pm 0.52) \times 10^{24}$ erg, corresponding to a conversion rate of $(2.20 \pm 0.29) \times 10^{22}$ erg s^{-1}, while the secondary detections had an average magnetic energy difference of $(3.10 \pm 0.46) \times 10^{24}$ erg with an energy conversion rate of $(1.38 \pm 0.28) \times 10^{22}$ erg s^{-1}.

Since the magnetic energies were calculated for the 14 stronger EBs, the radiative energies were taken for the same 14 detections for a direct comparison. Directly comparing the magnetic energy differences to the radiative energy of the detections in Hα over the same times, we find larger radiative energy to magnetic energy differences on average. This can be explained by some of the EBs being fueled during their lifetimes by new flux emergence or areas of moving magnetic flux. This addition of more magnetic flux will decrease the measured magnetic energy difference within the box, but not the measured radiative energy in Hα.

The temperature increase at the detection sites was also investigated. All 14 detections show enhancements in temperature at the detection site in the frame of initial detection, compared to the same location 6 scans ($\approx$265 s) prior to the initial detection. The temperature increases range from 40 to 570 K, with a mean enhancement of 200 K at the detection footpoints (optical depth of log(τ_{6302}) = -1, corresponding to an estimated mean physical height of 200 km from the NICOLE output model). The morphology of the temperature enhancements do not appear to follow the shape of the EB in Hα and is more characteristic of the EB footpoints.

5. EB PAIRING

Zachariadis et al. (1987) noted that EBs can appear and disappear in groups, usually formed a chain-like pattern with a separation distance of 1″–7″. The EBs had apparent horizontal motions of 0.6 km s^{-1}. This pairing of EBs was assumed to be connected to footpoints of magnetic loops caused by emerging

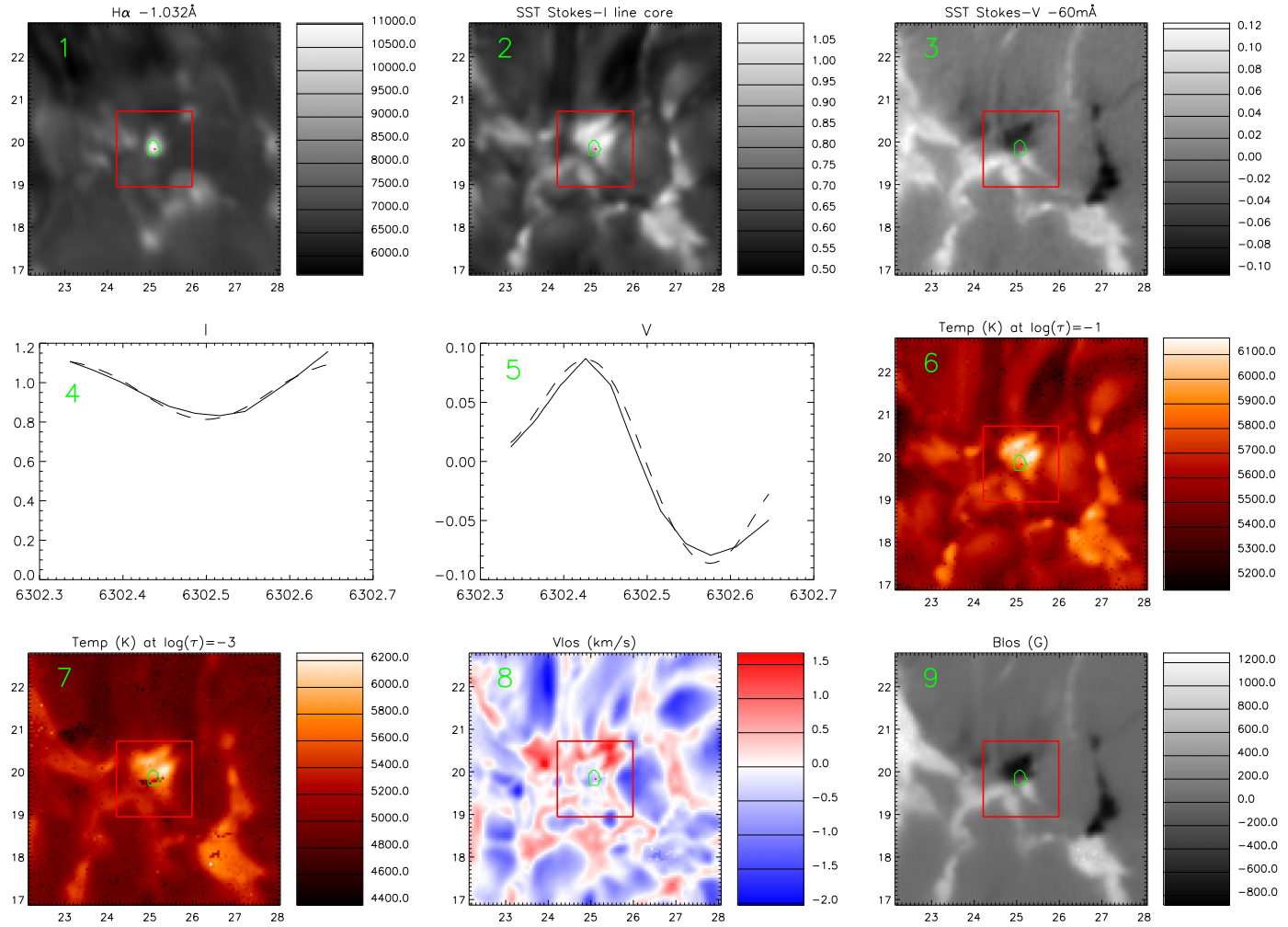

Figure 3. Panel (1): the SST observations in Hα −1.032 Å of an example EB. Panel (2): co-spatial Fe I 6302 Å line core Stokes-*I* imaging. Panel (3): co-spatial Fe I 6302 Å −60 mÅ Stokes-*V* imaging. Panel (4): the Stokes-*I* line profiles of the observations (solid) and the synthetic, fitted profiles from the inversions (dashed). The line profiles are taken from a pixel containing strong magnetic field within the red box. Panel (5): the Stokes-*V* line profiles, co-spatial to Stokes-*I*. Panel (6): the NICOLE output model showing the temperature at $\log(\tau) = -1$ (corresponding to esitmated height of 220 km). Panel (7): the temperature at $\log(\tau) = -3$ (corresponding to esitmated height of 670 km). Panel (8): line-of-sight velocity in the upper photosphere (positive—upflow). Panel (9): the line-of-sight magnetic flux density in the upper photosphere. The green contours show the detected area of the EB from EBDATA.

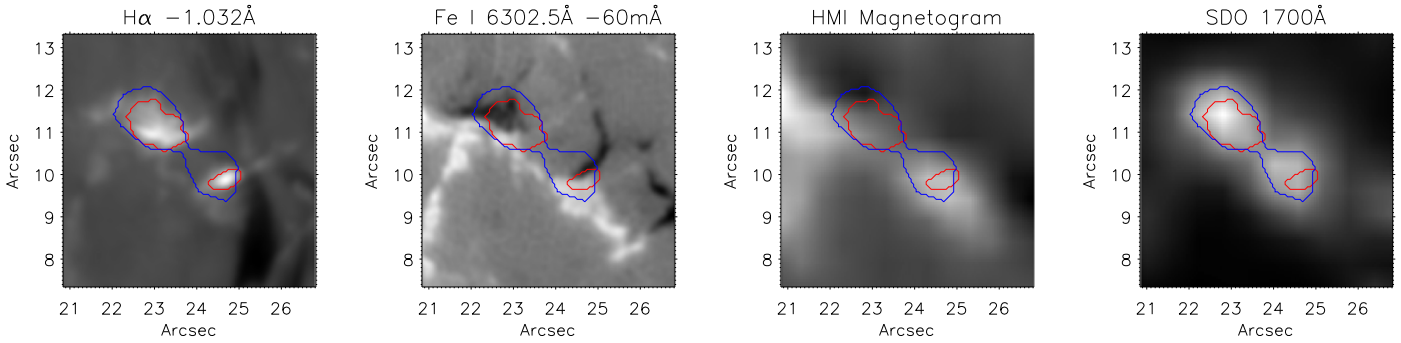

Figure 4. Example of an EB pair flaring. The area within the blue contour contains pixels that were greater than 5σ in the 1700 Å continuum with the red contour highlighting the detections from EBDATA in Hα.

(An animation of this figure is available.)

flux regions. This fits in with the resistive, undulatory "sea serpent" flux emergence mechanism for EB formation described by Georgoulis et al. (2002) and Pariat et al. (2004). Nelson et al. (2015) and Reid et al. (2015) have also shown that EBs can split apart, forming multiple paired EBs. The splitting occurred with a velocity of roughly 6 km s^{-1}, although the separation distance in these cases would be much smaller than that of Zachariadis et al. (1987).

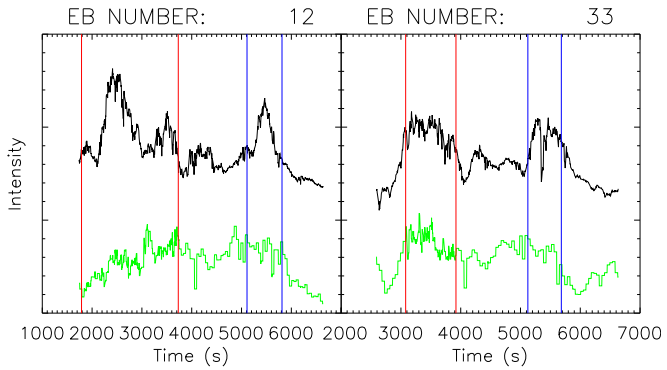

Figure 5. Light curves of EB012 (left) and EB033 (right). The black light curves (top lines) show the Hα −1.032 Å emission over time, inside the boxes described in the text. The green light curves (bottom lines) show the Fe I 6302.5 Å −60 mÅ Stokes-V absolute intensities over time inside the boxes. The red lines show the start and end detection times of these EBs. The blue lines show the start and end times for the later resurged EB detections 091(left) and 092 (right).

Our data set shows three instances where EBs are paired, corresponding to roughly 5% of all EBs in the data set. Figure 4 shows one of those with a mean separation of 2″. The origin of the EBs seem to arise from two areas of negative polarity magnetic flux simultaneously emitted from the sunspot which are traveling at a measured transverse velocity of 2.5–3.5 km s^{-1}. The areas of moving magnetic flux then approach a stationary area of opposite polarity magnetic flux with an EB appearing at both magnetic inversion lines when the opposite polarities meet (see attached Movie). The interactions of the bipolar areas slow the movement of the emitted negative polarity magnetic flux. By comparing the Fe I 6302.5 Å −150 mÅ Stokes-I images with the −60 mÅ Stokes-V/I images of the pairing, it appears as though granular movements affect the movement of the flux regions. Following the appearance of the EBs when the two polarities meet, the faster negative patches for each EB slow down to apparent velocities of 0.6 km s^{-1} and 0.8 km s^{-1} while still moving away from the sunspot.

The paired EBs are also detected by EBDATA, labeled as 012 and 033, with lifetimes of 1942 and 841 s, respectively, and were categorized as primary detections for inversion purposes. Detection 012 has a much longer lifetime due to the area of stationary, positive polarity flux associated with this EB being much closer to the sunspot, and so the bipole forms before detection 033. Figure 5 shows the Hα −1.032 Å and Fe I 6302.5 Å −60 mÅ Stokes-V absolute intensity of each of the detections over time. These light curves were measured by placing a 10 pixel^2 box around the initial detection area for each EB. The EB was then tracked throughout its lifetime, with the position of the box following the central position of each detection. When the EBs faded and were no longer detected by EBDATA, their associated bipoles were then tracked. The negative polarity flux region within the bipole associated with detection 012 is fueled by further flux emergence moving out of the sunspot. The fueling of the negative polarity region occurs at least twice where it is noticeable, with roughly 900 s between fueling events (the first of which occurs at $T = 2200$ s and the negative polarity flux is still emanating out from the sunspot, while the second fueling is noticeable by the large spike in Stokes-V signal at $T = 3100$ s). The measured flux cancellation rates were $(-2.36 \pm 1.14) \times 10^{14}$ Mx s^{-1} and $(1.27 \pm 0.16) \times 10^{14}$ Mx s^{-1}, respectively, for the detections. The negative value here is due to the fueling of 012. These detections then fade out as the bipolar regions weaken due to the flux cancellation. After 012 and 033 have extinguished, more negative polarity flux emergence from the sunspot fuels the EB areas. At 1190 s after the last frame detecting 012 and 033, two further detections are also made which are related to the resurgence of these EBs caused by the flux emergence interacting with the positive polarity existing flux in the area, forming two new bipoles. The refueling of the detections is not periodic.

Flaring in the wings of Hα related to the new EBs are labeled as 091 and 092, which have flux cancellation rates of $(5.76 \pm 0.76) \times 10^{14}$ Mx s^{-1} and $(5.90 \pm 0.78) \times 10^{14}$ Mx s^{-1}, respectively, which are measured through inversions. The new detections have lifetimes of 702 and 559 s, respectively, as shown by the blue bars in Figure 5. The areas of opposite polarity magnetic flux connected to detection 091 lengthen, and by the end of its lifetime the magnetic flux tied to the detection contains only negative polarity flux. This lengthening of the areas of opposite polarity flux is similar to that noted previously (Reid et al. 2015) where the bipole connected to the EB was constrained to the intergranular lanes, forming long, thin regions of magnetic flux. Detection 092 disappears at roughly the same time, although the line-of-sight magnetic fields show a more intricate story. Negative polarity flux connected to 092 seems to split off, with some of the flux staying with the detection and the rest connecting to a different region of the same polarity magnetic flux. This could be due to granular buffeting of the magnetic flux regions, causing a destabilization of the bipoles. The detection loses a large proportion of its magnetic potential energy, and 092 becomes extinct shortly afterward. Following extinction, only the positive polarity magnetic fields connected to this detection remain, with the negative polarity magnetic flux region away from detection area still visible.

A second pairing of EBs is also present in the data set, although in this case, the paired system contains a triplet of EBs. Unfortunately, these EBs only appear toward the end of the observations and are not seen in their entirety, and flux cancellation rates cannot be calculated. All three EBs are picked up by EBDATA and would have been classified as primary EBs because they passed the *SDO* 1700 Å test. Each EB within the triplet is formed by negative magnetic flux emerging from the penumbral region of the sunspot and moving out into the surrounding photosphere where the regions are all met with existing positive polarity areas of photospheric magnetic flux. The apparent transverse motions of the negative polarity patches prior to the EBs flaring have velocities of 2.9–3.6 km s^{-1}. The EBs in the triplet only begin to appear in Hα when the opposite polarity areas meet, that is, 5 minutes before the observations end. It was possible to obtain an estimate for the apparent transverse velocity of the EBs in the triplet. This was found to be 0.6–1.1 km s^{-1}.

6. DISCUSSION AND CONCLUSIONS

We have developed EBDATA. A skeleton version of this code was adapted to test its functionality in comparison with other existing codes. This resulted in finding a similar amount of EB detections arcsec^{-2} s^{-1} as in previous studies (Nelson et al. 2013a; Vissers et al. 2013). Using the co-aligned spectro-polarimetric data from the SST, it was shown that the code

produced a higher proportion of strong, bipolar detections when an impulsive criterion was applied. This reduced the number of false positives where a moving magnetic region in the photosphere would show up as brightening in the Hα line wings and would fade into the intensity thresholding set in the detection criteria. The algorithm produced results very similar to those of Vissers et al. (2013), with the impulsivity aspect of our algorithm reducing the number of short-lived transient brightenings classified as detections.

Using intensity thresholding of co-aligned *SDO* 1700 Å data, 14 of the strongest EB detections from EBDATA were selected for inversions. The 6302.5 Å spectro-polarimetric data of these detections were ran through the NICOLE inversion code to find local magnetic flux and temperatures. The line-of-sight magnetic flux density from the output models of the inversions show that the area around the detections had an average flux cancellation rate of $(9.17 \pm 1.26) \times 10^{14}$ Mx s^{-1}. Interestingly, when only considering the weaker, secondary set of detections, which had *SDO* 1700 Å intensities ranging from 5σ–6σ above background average, the average flux cancellation rate was $(7.73 \pm 1.13) \times 10^{14}$ Mx s^{-1}, indicating that the stronger the intensity in 1700 Å, the stronger the flux cancellation rate.

Inversion tests show that fits including stray light vary strongly on a pixel by pixel basis. This shows that spatially coupled inversions are a highly desirable feature for future development as stray light is a major component in all observational data.

A comparison of the line-of-sight magnetograms from HMI with our 14 SST detections shows that the HMI magnetograms at the magnetic inversion line struggle with the low resolution to fully resolve the bipole, and are therefore less reliable for the study of small-scale photospheric magnetic bipoles. The higher spatial resolution SST spectropolarimetric data provided clearer information on the bipoles with good seeing which, when inverted, gave less noisy, crisper results for flux cancellation rates on the small-scale bipoles. However, the HMI measurements seemed to give values of flux cancellation similar to the inverted SST measurements, and could suffice for this purpose. However, without fully resolving the bipole, it would be extremely difficult to ascertain if any fueling was interfering with the HMI results, or to attain any small-scale structuring of the bipolar regions under investigation.

EB energies in the literature have been reported to range from 10^{22} to 10^{28} erg. Using Equation (2) to work out the radiative energy rates from the 116 detections in Hα, and integrating these across the detection lifetimes, we find that the resultant energies are 10^{23}–10^{26} erg. These energies are mostly similar to those found by Nelson et al. (2013a). Georgoulis et al. (2002) found energies of 10^{26}–10^{28} erg. These were found to be much higher, possibly due to the constant lifetime of $D = 600$ s as well as the apparent area of the EBs being much larger than the areas we observe in Hα. Using the output models from the inversions of the 14 strong EBs, we find magnetic energy differences of 10^{24}–10^{25} erg over an average time of 500 s, which corresponds to magnetic energy conversion rates of $\approx 10^{22}$ erg s^{-1}.

Direct comparison of the magnetic and radiative Hα energies shows that the radiative energy only accumulates up to 31.2% of the magnetic energy difference for the EBs. Here, we note that 5 of the 14 inverted detections were removed from consideration because they contained apparent refueling in their lifetimes. Without removing EBs, which are refueled over their lifetime, the average radiative energy would be higher than the magnetic energy difference. Not all of the magnetic energy that disappears will convert to radiative energy. Some of the magnetic energy will also convert to kinetic energy.

Similar to the flux cancellation rates, the stronger, primary EBs had higher values for magnetic energy conversion rates than the secondary subset. The primary detections had an average peak intensity that was 163% that of the background Hα, while the secondary detections had an average peak intensity of 148% (values obtained via the output of EBDATA mentioned in Section 3). This implies that the higher the magnetic energy conversion rate, the brighter the detection appears, and this conversion rate could determine the brightness of the EBs.

As is evident in Figure 5, flux cancellation and magnetic energy conversion rates may be impacted by the fueling of EBs, and it cannot be claimed that the stronger the measured flux cancellation/magnetic energy, the brighter an individual EB will definitely appear in Hα/*SDO* 1700 Å. Another potential issue is that some EBs have been observed to have their magnetic inversion line lengthen, as seen Section 5 and Reid et al. (2015). This lengthening may alter the flux cancellation rates and will most definitely alter the Hα wing emission. If the flux cancellation is spread out, then the average intensity in Hα would also weaken. Therefore, while the flux cancellation values could be similar within the box as a whole, if it is more localized inside the measured box, then the brightness in Hα should also be more concentrated.

The inversions also show a temperature increase at the EB locations. This increase was found to be on average 200 K at a mean height of 200 km above the photospheric floor (log $(\tau) = -1$), compared to the local area prior to the detection. This is lower than some previous studies using Hα and Ca II 8542 Å data (Georgoulis et al. 2002; Fang et al. 2006; Isobe et al. 2007; Archontis & Hood 2009), which may show an increase in temperature closer to the middle of the EB detection height. The temperature estimates presented in this paper are on the extreme lower end of the newer research provided by co-observations with IRIS using lines more sensitive to higher temperatures (Peter et al. 2014; Kim et al. 2015; Vissers et al. 2015), which suggest that EBs may have temperature ranges up to 80,000 K underneath the chromospheric canopy. The low temperature enhancements we find in comparison are most likely due to our diagnostic line sampling the footpoints of the EBs. The inversions indicate that at a height of 750 km (log $(\tau) = -3.5$), the mean temperature enhancement rises to 500 K. This result may not be fully reliable due to the low formation height of the Fe I 6302 Å line. However, this does indicate that the higher areas are heated more than the lower photosphere. This fits with the recent study of Vissers et al. (2015), which indicates that the tops of the EBs may be the hottest regions. With only Fe I 6302.5 Å and Hα, we are unable to attain any information corresponding to these very high temperatures.

EB pairs have also been found. The pairs were all formed when groups of negative polarity magnetic flux were emitted from a sunspot. The flux traveled away from the sunspot at a velocity of 2.5–3.5 km s^{-1}. When this flux came into contact with existing, stationary opposite-polarity flux, the EBs were formed at the magnetic inversion lines. The movement of the bipoles was much slower than the initial, unhindered negative polarity flux, with a velocity of 0.6–1.1 km s^{-1}, which is the same as the Hα measured transverse velocity of the EBs. This

velocity matches well with the previous transverse velocity estimates of Zachariadis et al. (1987).

We thank an anonymous referee for useful comments and suggestions. Armagh Observatory is grant-aided by the N. Ireland Department of Culture, Arts and Leisure. The Swedish 1 m Solar Telescope is operated on the island of La Palma by the Institute for Solar Physics of Stockholm University in the Spanish Observatorio del Roque de los Muchachos of the Instituto de Astrofísica de Canarias. The authors acknowledge the DJEI/DES/SFI/HEA Irish Centre for High-End Computing (ICHEC) for the provision of computing facilities and support. We acknowledge support by STFC. This research was supported by the SOLARNET project (www.solarnet-east.eu), funded by the European Commissions FP7 Capacities Program under grant agreement 312495. The research leading to these results has received funding from the European Community's Seventh Framework Programme (FP7/2007–2013) under grant agreement No. 606862 (F-CHROMA). E.S. is a Government of Ireland Post-doctoral Research Fellow supported by the Irish Research Council.

REFERENCES

Archontis, V., & Hood, A. W. 2009, A&A, 508, 1469
Berlicki, A., & Heinzel, P. 2014, A&A, 567, A110
Brown, J. C. 1973, SoPh, 39, 421
Bruzek, A. 1972, SoPh, 26, 94
Danilovic, S., Gandorfer, A., Lagg, A., et al. 2008, A&A, 484, L17
Dara, H. C., Alissandrakis, C. E., Zachariadis, T. G., & Georgakilas, A. A. 1997, A&A, 322, 653
de la Cruz Rodrguez, J., & Piskunov, N. 2013, ApJ, 764, 33
de la Cruz Rodríguez, J., Löfdahl, M., Sütterlin, P., Hillberg, T., & Rouppe van der Voort, L. 2015, A&A, 573, A40
Ellerman, F. 1917, ApJ, 46, 298
Fang, C., Tang, Y. H., Xu, Z., Ding, M. D., & Chen, P. F. 2006, ApJ, 643, 1325
Fontenla, J. M., Avrett, E. H., & Loeser, R. 1993, ApJ, 406, 319
Georgoulis, M. K., Rust, D. M., Bernasconi, P. N., & Schmieder, B. 2002, ApJ, 575, 506
Hashimoto, Y., Kitai, R., Ichimoto, K., et al. 2010, PASJ, 62, 879
Henriques, V. M. J. 2012, A&A, 548, A114
Hong, J., Ding, M., Li, Y., Fang, C., & Cao, W. 2014, ApJ, 792, 13
Isobe, H., Tripathi, D., & Archontis, V. 2007, ApJL, 657, L53
Judge, P. G. 2015, ApJ, 808, 116
Kim, Y., Yurchyshyn, V., Bong, S., et al. 2015, ApJ, 810, 38
Kitai, R. 1983, SoPh, 87, 135
Lemen, J. R., Title, A. M., Akin, D. J., et al. 2012, SoPh, 275, 17
Li, Z., Fang, C., Guo, Y., Xu, Z., & Cao, W. 2015, RAA, 15, 1513
Litvinenko, Y. E. 1999, ApJ, 515, 435
Matsumoto, T., Kitai, R., Shibata, K., et al. 2008a, PASJ, 60, 95
Matsumoto, T., Kitai, R., Shibata, K., et al. 2008b, PASJ, 60, 577
Nagai, F. 1980, SoPh, 68, 351
Nelson, C., Scullion, E. M., Doyle, J. G., Freij, N., & Erdélyi, R. 2015, ApJ, 798, 19
Nelson, C. J., Doyle, J. G., Erdelyi, R., et al. 2013a, SoPh, 283, 307
Nelson, C. J., Shelyag, S., Mathioudakis, M., et al. 2013b, ApJ, 779, 125
Pariat, E., Aulanier, G., Schmieder, B., et al. 2004, ApJ, 614, 1099
Pariat, E., Schmieder, B., Berlicki, A., et al. 2007, A&A, 473, 279
Peter, H., Tian, H., Curdy, W., et al. 2014, Sci, 346, 1255726
Reid, A., Mathioudakis, M., Scullion, E., et al. 2015, ApJ, 805, 64
Rutten, R. J. 2003, Radiative Transfer in Stellar Atmospheres (Utrecht: Utrecht Univ.)
Rutten, R. J., Vissers, G. J. M., Rouppe van der Voort, L. H. M., Sutterlin, P., & Vitas, N. 2013, JPhCS, 440, 012007
Scharmer, G. B., Bjelksjo, K., Korhonen, T. K., Lindberg, B., & Petterson, B. 2003, Proc. SPIE, 4853, 341
Scharmer, G. B., Henriques, V. M. J., Kiselman, D., & de la Cruz Rodrguez, J. 2011, Sci, 333, 316
Scharmer, G. B., Narayan, G., Hillberg, T., et al. 2008, ApJL, 689, L69
Scherrer, P. H., Schou, J., Bush, R. I., et al. 2012, SoPh, 275, 207
Schmieder, B., Rust, D. M., Georgoulis, M. K., Démoulin, P., & Bernasconi, P. N. 2004, ApJ, 601, 530
Schnerr, R. S., de La Cruz Rodríguez, J., & van Noort, M. 2011, A&A, 534, A45
Socas-Navarro, H., de la Cruz Rodriguez, J., Asensio Ramos, A., Trujillo Bueno, J., & Ruiz Cobo, B. 2015, A&A, 577, A7
Socas-Navarro, H., Martnez Pillet, V., Elmore, D., et al. 2006, SoPh, 235, 75
Socas-Navarro, H., Ruiz Cobo, B., & Trujillo Bueno, J. 1998, ApJ, 507, 470
Socas-Navarro, H., & Trujillo Bueno, J. 1997, ApJ, 490, 383
van Noort, M. 2012, A&A, 548, A5
van Noort, M., Rouppe van der Voort, L., & Löfdahl, M. G. 2005, SoPh, 228, 191
van Noort, M. J., & Rouppe van der Voort, L. H. M. 2008, A&A, 489, 429
Vissers, G. J. M., van der Voort, L. H. M., & Rutten, R. J. 2013, ApJ, 774, 32
Vissers, G. J. M., van der Voort, L. H. M., Rutten, R. J., et al. 2015, ApJ, 812, 11
Watanabe, H., Kitai, R., Okamoto, K., et al. 2008, ApJ, 684, 736
Watanabe, H., Vissers, G., Kitai, R., van der Voort, L. R., & Rutten, R. J. 2011, ApJ, 736, 71
Yang, H., Chae, J., Lim, E.-K., et al. 2013, SoPh, 288, 39
Zachariadis, T. G., Alissandrakis, C. E., & Banos, G. 1987, SoPh, 108, 227